JOURNAL OF SYNCHROTRON RADIATION

ISSN 1600-5775

Early commissioning results for spectroscopic X-ray Nano-Imaging Beamline BL 7C sXNI at PLS-II

Sangsul Lee,[a] Ik hwan Kwon,[b] Jae-Young Kim,[a] Sung-Sun Yang,[c] Sechang Kang[d] and Jun Lim[a]*

[a]Industrial Technology Convergence Center, Pohang Light Source, Pohang 37673, South Korea, [b]Department of Physics, POSTECH, Pohang 37673, South Korea, [c]VACTRON Co. Ltd, 37-30 Maeyeo-ro, Deagu 41059, South Korea, and [d]KVAC Co. Ltd, 210 NINT 77 Cheongam-ro, Pohang 37673, South Korea. *Correspondence e-mail: limjun@postech.ac.kr

Received 5 May 2017
Accepted 27 September 2017

Edited by Y. Amemiya, University of Tokyo, Japan

Keywords: X-ray nano-imaging; tomography; XANES imaging; battery.

For spectral imaging of chemical distributions using X-ray absorption near-edge structure (XANES) spectra, a modified double-crystal monochromator, a focusing plane mirrors system and a newly developed fluorescence-type X-ray beam-position monitoring and feedback system have been implemented. This major hardware upgrade provides a sufficiently stable X-ray source during energy scanning of more than hundreds of eV for acquisition of reliable XANES spectra in two-dimensional and three-dimensional images. In recent pilot studies discussed in this paper, heavy-metal uptake by plant roots *in vivo* and iron's phase distribution in the lithium–iron–phosphate cathode of a lithium-ion battery have been imaged. Also, the spatial resolution of computed tomography has been improved from 70 nm to 55 nm by means of run-out correction and application of a reconstruction algorithm.

1. Introduction

Zone-plate-based hard-X-ray full-field transmission X-ray microscopy (TXM) is powerful in that it can probe large-volume materials as well as biological samples to high spatial resolution (down to 20 nm) and high contrast by use of Zernike phase contrast (Chen *et al.*, 2011; Vila-Comamala *et al.*, 2012). Recently, to achieve higher-than-TXM resolution, point-by-point beam scanning or sample scanning such as ptychography (Shapiro *et al.*, 2014) and scanning transmission X-ray microscopy (Nazaretski *et al.*, 2015) have been utilized. Notwithstanding, TXM remains the most effective tool for research of various arbitrary-shaped samples. In fact, over the past few years since the introduction of chemically sensitive high-resolution X-ray absorption near-edge structure (XANES) imaging (Rau *et al.*, 2003; Meirer *et al.*, 2011; Wang *et al.*, 2014), its applicability has been extended to the study of battery materials. Because XANES is sensitive to probed elements' chemical and local-electron-charge changes, it has been extensively exploited for characterization of fine-structural change in a large variety of materials. XANES is a synchrotron-radiation-limited technique in that it requires a broadband of X-rays, that is, a wide band that can cover the absorption *K*-edge of transition metals from 5 to 20 keV with a high energy resolution of ~0.1 eV. Currently there are few active beamlines incorporating TXM with XANES: BL 6C (wiggler source) at Stanford Synchrotron Radiation Light Source (Kuppan *et al.*, 2017), X8C (bending-magnet source) at the National Synchrotron Light Source (Wang *et al.*, 2014), NANO beamline (wiggler source) at ANKA (Bauer *et al.*, 2015) and 32-ID (undulator source) at the Advanced Photon

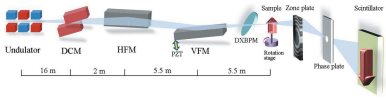

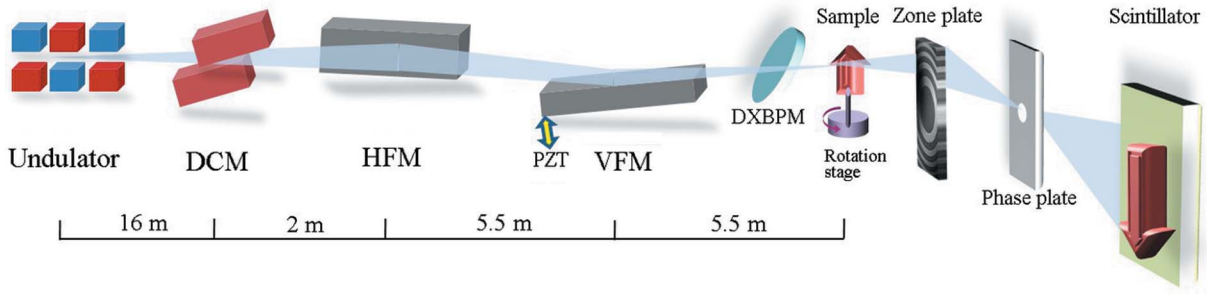

Figure 1
Schematic of the new sXNI beamline at PLS-II.

Source (Andrade *et al.*, 2016). In order to measure accurate chemical information [$\ln(I/I_0)$], X-rays must have a broad energy range, constant intensity and stable positioning, because TXM cannot image the background (I_0) and sample (I) simultaneously. Those beamlines' sources meet these prerequisites. Until recently, the 7C X-ray Nano-Imaging (XNI) beamline at Pohang Light Source II (PLS-II) was dedicated only for high-resolution computed tomography (CT) utilizing undulator radiation. Also, there were no beam deflection optics or beam-position feedback system. This paper shows how 7C XNI was upgraded for reliable chemically mapped imaging and improved CT results.

2. Beamline overview

The 7C XNI beamline was constructed in 2011 for coherent imaging and high-resolution full-field tomography (Lim *et al.*, 2014). Initially, for focusing of X-rays, beryllium parabolic compound refractive lenses (CRLs) were installed instead of reflecting mirrors. The X-ray energy was fixed at 6.75 keV to obtain the Zernike phase contrast *via* a holed aluminium-film phase plate of 3.78 µm thickness (phase delay: $\pi/2$). Beamline 7C XNI offers outstandingly high contrast for low-Z-material specimens such as biological cells, polymers and carbon materials, among others. For imaging, a tungsten objective zone plate of 40 nm outermost zone width, 150 µm diameter and 0.6 µm thickness (Zoneplates, UK) is utilized. As a detector, a scintillator-coupled optical microscope of thin scintillation crystal (15 µm-thick Tb:LSO, FEE) with a 20× optical objective and a large-area CCD (U16MF, Apogee) of 4096 × 4096 sensors with 9 µm square pixels is used. In 2015, in order to obtain chemically mapped images, a rhodium-coated horizontal focusing plane mirror (HFM; 1250 mm long) and a vertical focusing plane mirror (VFM; 600 mm long) were installed. Additionally, the liquid-nitrogen-cooled double-crystal monochromator (DCM) was modified and a beam-position feedback system was installed for stabilization of beam movement. Fig. 1 shows a schematic of the new beamline.

2.1. Mirror system

The CRLs are chromatic optics, the focal position of which is a function of X-ray energy. Compared with CRLs, focusing plane mirrors, despite the fact that they are 20 times more expensive, have some advantages. First, they are achromatic optics, which means that the focal position, which should be attained for tomography with X-ray energy tunability, is not dependent on X-ray energy. Second, the focal position is adjustable by use of a mirror bender system (Vactron Co. and KVAC Co., Korea); this provides room in which to change the sample position if necessary. Typically, the radius of curvature of the mirrors varies from flat to ∼1 km. In our case, in order to set the focus at 29 m downstream from the source, the radius of curvature of the HFM and VFM are set to 3.41 km and 2.23 km, respectively, when the incidence angle is 4 mrad. The measured value of the focused beam size is 260 µm (horizontal) × 15 µm (vertical), the related photon flux is 2.6×10^9 photons µm^{-2}, and the demagnification factors horizontally and vertically are 1.64 and 4.27, respectively (Fig. 2). Interestingly, in the case of the CRLs, the focused beam flux is 2.0×10^9 photons µm^{-2} when the demagnifica-

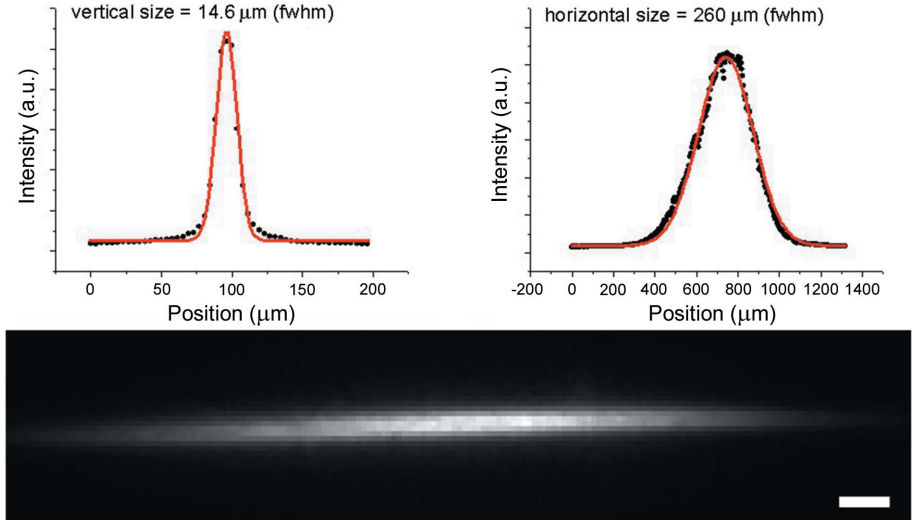

Figure 2
Focused beam image and line plots at the sample position. The scale bar is 30 µm.

tion factor is 7.79, and the focused beam size is 70 µm (horizontal) × 8 µm (vertical). Even though, in our case, the mirror bender system offers no gain in photon flux relative to the CRLs, its full-field high-resolution imaging with high-resolution energy scanning at a fixed focal position enables us to obtain detailed chemical information.

2.2. Upgraded cryogenically cooled DCM

In the PLS-II upgrade project (2009–2011), PLS and Vactron Co. (http://www.vactron.co.kr) developed a liquid-nitrogen-cooled DCM and planned to install it for all insertion device beamlines at PLS-II. In 2011, ten DCM sets were installed. The design follows the typical concept of the vertical bounce and fixed first crystal. It incorporates a pair of Si (111) crystals and can deliver a monochromatic 5–20 keV beam with a nominal vertical offset of 25 mm. The crystals are mounted on a common rotational Bragg shaft, which ensures that they rotate synchronically when the Bragg angle is changed. In order to remove the second crystal's translation motion (so-called Z2) in the beam direction, a 150 mm-long crystal was installed. In the original design, the pitch and roll motions of the second crystal were driven by two small linear-actuators (picomotor actuator 8302-UHV, Newport) for coarse-movement functionality and two tiny PZT actuators (P-843; Physik Instrumente) for fine adjustment, and each motion was monitored by two LVDT sensors. Also, a long-travel-length (20 mm) and high-driving-force (600 N) piezo actuator (N-216 NEXLINE; Physik Instrumente) was utilized for upward translation motion (so-called Y2). The mechanism of the first version was not well designed for minimization of the vibration and drift of the second crystal. Moreover, it did not meet the requirement of the fixed beam exit during X-ray energy scanning. Therefore, in the present upgrade, in order to preserve the beam stability and provide for the fixed beam exit with changing X-ray energy, the second crystal motion's mechanical design was modified. Fig. 3 shows a three-dimensional CAD drawing of the original and modified main components of the DCM. The concept of the new design is based on a decreased number of actuators as well as minimized second crystal vibration and drift based on the incorporation of stiffening plates. The new DCM has one linear stage (MVXA16A, Kohzu) for Y2 motion and two piezo actuators (N-216) for second crystal pitch and roll motions. The second crystal supporting block is compact and robust, and is on the Y2 linear stage.

In the original design, both the first and second crystals are cooled: the first crystal directly by the Cu block and the second crystal by Cu braid connections to the Cu block of the first crystal. We noted that, when the second crystal is in motion, the Cu braid connection imparts an unbalanced holding force, which causes unstable beam direction and intensity fluctuation. In the new design, therefore, there is neither any Cu braid connection nor any cooling mechanism for the second crystal. Since the DCM's installation in 2015, there has been no evidence of any thermal issue. To prove its parallelism performance, we measured diverging (no bending, both mirrors) monochromatic beam movement for energy adjustments between 5 and 16 keV, using the scintillator-coupled optical microscope at the sample position. The beam size, 500 µm (horizontal) × 500 µm (vertical), was defined by the slit in front of the DCM. As shown in Fig. 4(*a*), the pitch angle varies gradually, and the total variation is ∼60 µrad (12 arcsec). At 5–6 keV (Bragg angle: 23–19°), there can be an abrupt change of center of mass or Y2 motion error. This conclusion is supported by the results of another measurement: by use of the calibrated LVDT sensors, we determined that the second crystal's angle variation is ∼100 µrad (20 arcsec) in pitch and ∼30 µrad (6 arcsec) in roll [Fig. 4(*b*)]. Even though there are steep variations at a specific energy, in the 5–15 keV region of interest range, the total variation is

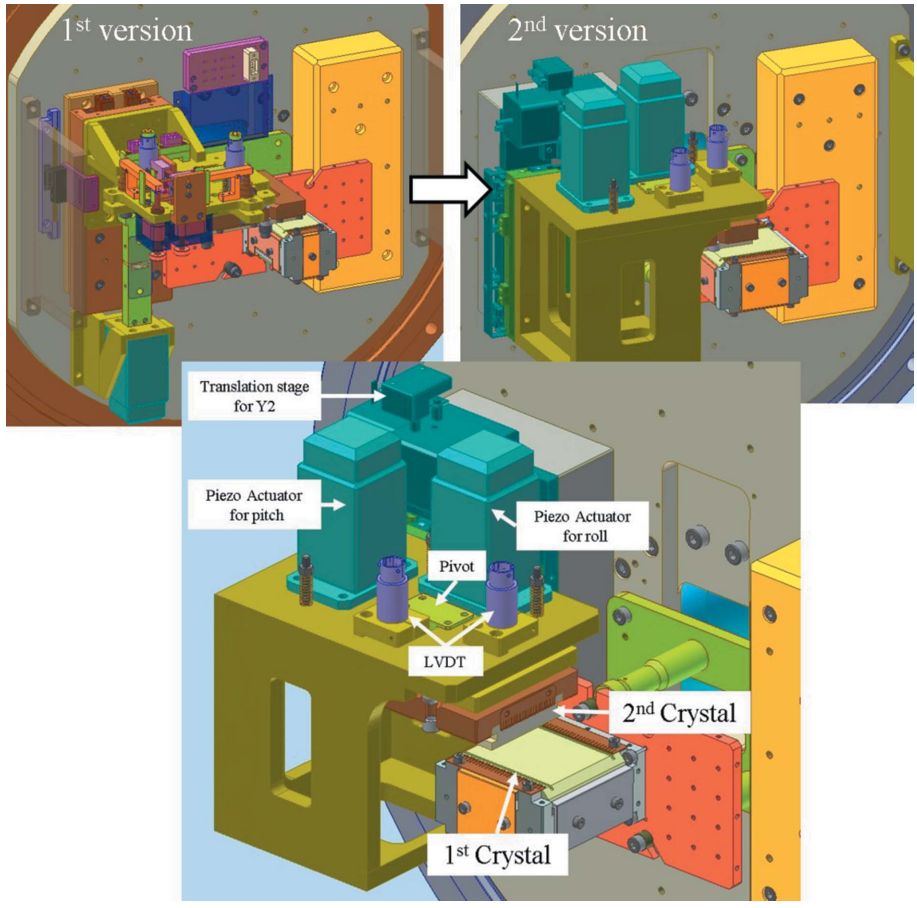

Figure 3
Three-dimensional CAD drawing of the original and modified main components of the DCM.

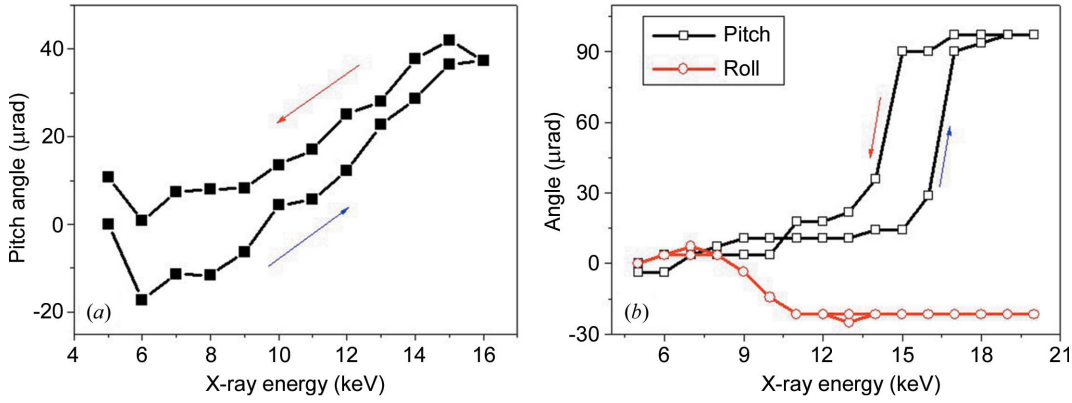

Figure 4
Monochromatic beam movement as a function of energy from 5 to 16 keV. (*a*) Graph of vertical beam changes (converted to pitch angle) measured by the imaging detector. (*b*) Graph of the second crystal's pitch and roll angle changes measured by LVDT.

only 15 μrad (3 arcsec) in pitch. Note that due to uncertainty in the horizontal beam movement measurement and its low importance, roll motion error is not discussed herein. Certainly, roll motion does not result in any evident beam movement in the horizontal direction. And if we assume that the first crystal shows no error in motion, the second crystal's pitch variation is equal to the parallelism variation of the crystals. However, in truth, the error is not negligible; thus, if credible XANES spectrum images are to be obtained, beam movement should be adjusted for by use of a beam feedback system. In any case, we are confident that the performance is comparable with that of other commercial DCMs.

2.3. X-ray beam-position monitoring and feedback system

The upgraded beamline requires an X-ray beam-position monitor and feedback system to keep the beam position constant on the sample. The beam stability is crucial, as there are no means of obtaining the background image (I_0) and sample image (I) simultaneously with a two-dimensional detector. Thus, we developed a direct X-ray beam-position monitor (DXBPM) with a position resolution of ∼1.0 μm by use of a fluorescence diamond screen. The commercial X-ray diamond beam-position monitor (DBPM) can measure the focused beam position to a resolution of less than 10 nm. However, because it is made up of four pads separated by 1–20 μm gaps, it inevitably blocks some part of the beam. Also, high-resolution motorized stages are required to determine the position calibration factor, which should be varied when the beam size is changed. Due to the limited working range (less than 100 μm) moreover, its position has to be re-adjusted when the beam is out of range. The DXBPM, contrastingly, is simple and has no such drawbacks or constraints. Its hardware comprises a diamond screen and an optical microscope (Fig. 5). The fluorescence diamond screen is a boron-doped CVD diamond (30 μm-thick, 10 mm width; Diamond Materials GmbH). The fluorescence yield of the screen is sufficiently high for detection with a cheap CMOS

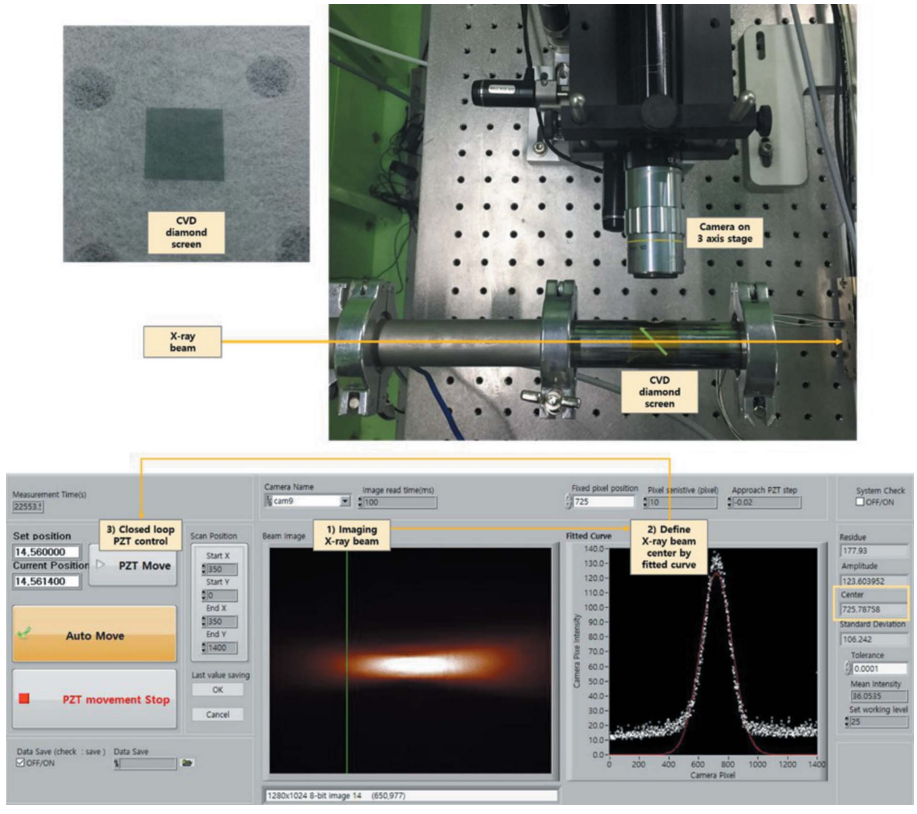

Figure 5
X-ray beam-position monitor and feedback system. DXBPM utilizes a fluorescence diamond screen (top left) and a low magnification optical microscope (top right). The *LabVIEW*-based feedback software controls the VFM pitch motion (bottom).

camera. By use of its 10× objective lens, the optical microscope has an effective pixel size of 0.5 µm. It acquires an image of the beam and then determines the peak position, regardless of size, in the vertical direction by Gaussian fit. It generates a feedback signal and adjusts the piezo actuator (P-845.20, 30 µm travel; Physik Instrumente GmbH) that is installed for VFM pitch motion (Fig. 1). The actuator can increase the pitch angle up to 50 µrad. Thereby, the feedback system, with its 1 s feedback loop, can control the parallelism error of the DCM.

3. Examples of scientific applications

3.1. 3D imaging of ruby powder

Recently, we developed an alignment method for correction of the axial and radial motion errors of the rotation stage in a tomography setup (Kwon *et al.*, 2016). The method uses a capillary tube as a sample holder and utilizes a halo artifact to correct the errors of the rotation stage. In 2017, we modified the method to enhance both spatial resolution and CT image contrast. First, for the spatial resolution enhancement, we fitted the summed pixel intensities along each axis by eighth-order nonlinear fit. After fine correction of the run-out errors of the rotation stage, the resolution was enhanced from 70 to 55 nm. Second, for the contrast improvement, we devised a new method of sinogram normalization. Note that, because we cannot take both background and sample images at the same time, background subtraction (or normalization) is incomplete; the result is a stripe pattern in the sinogram and degraded CT image contrast. Thus, we normalize the sinogram, directly and effectively, according to its background intensity. The result is improved contrast with diminishment of most CT image streak artifact. We will publish a report of this approach shortly. In the meantime, in order to verify the system performance, we imaged for the first time a ∼20 µm ruby sphere widely used for ruby-line spectroscopy. All natural rubies have internal defects, including color impurities and inclusions of rutile needles known as silk. Indeed, as can be seen in the 3D and CT images in Fig. 6, there are many rutile needles inside the ruby. The spatial resolution of the CT image, as evaluated by power spectrum analysis, is 55 nm.

3.2. Elemental imaging of plant roots *in vivo*

In the present upgrade, we employed elemental sensitive microscopy for material-science and variable scientific applications. Spectroscopic full-field TXM is a powerful tool for investigation of transition metals and phase-transformative elements, in that it captures millions of spectra (pixels of CCD) with tens of nanometers resolution, at once. In order to obtain an element-specific image, two images are required above and below the characteristic X-ray absorption edge. The difference determines the distribution of the corresponding elements in a sample (Grew *et al.*, 2010; Liu *et al.*, 2012). As an example, we took images of live maize roots in water contaminated with heavy metals. Persistent heavy-metal pollution with its toxic effects poses a major threat to all life forms. Bioremediation of hazardous metals, therefore, has received considerable and growing interest over the years. The technique utilizes inherent biological mechanisms in microorganisms and plants to eradicate hazardous contaminants and restore polluted environments to their original conditions. It is an environmentally friendly and cost-effective technique for heavy-metal removal/recovery, certainly when compared with the conventional chemical and physical techniques. To visualize heavy-metal uptake by plant tissue, we immersed maize roots (size: hundreds of micrometers) in iron (EDTA-Fe, 10 m*M*)-contaminated water. Fig. 7(*a*) shows a Zernike phase contrast image of the roots. In principle, it is difficult to distinguish whether a given part is thicker or if metal is present. However, the obtained iron-sensitive image [Fig. 7(*b*)], which reflects the difference between the images 20 eV above (*i.e.* at 7132 eV) and 20 eV below (*i.e.* at 7092 eV) the Fe *K*-edge (*i.e.* at 7112 eV), indicates clearly which part contained a significant amount of iron. As expected, the highly concentrated iron (red color) was distributed in the central vessel of the root. In the near future, we plan to obtain CT images for in-depth study of heavy-metal uptake in plants.

3.3. XANES imaging of a battery

The lithium iron phosphate ($LiFePO_4$) or LFP battery is a type of rechargeable lithium-ion battery that uses $LiFePO_4$ as a cathode material. LFP batteries have a somewhat lower energy density than the more common lithium cobalt oxide

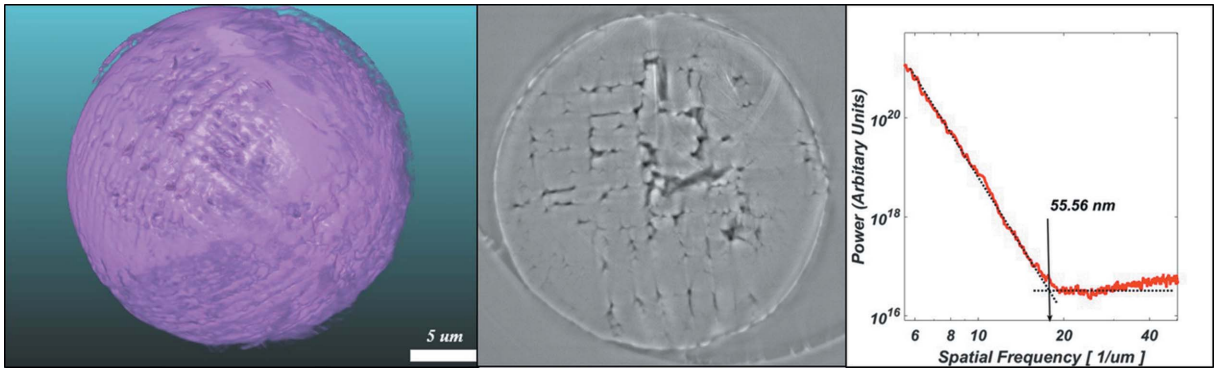

Figure 6
From left to right: volume 3D image, virtual slice image of the reconstructed tomography, and power spectrum of a slice of a 20 µm ruby sphere.

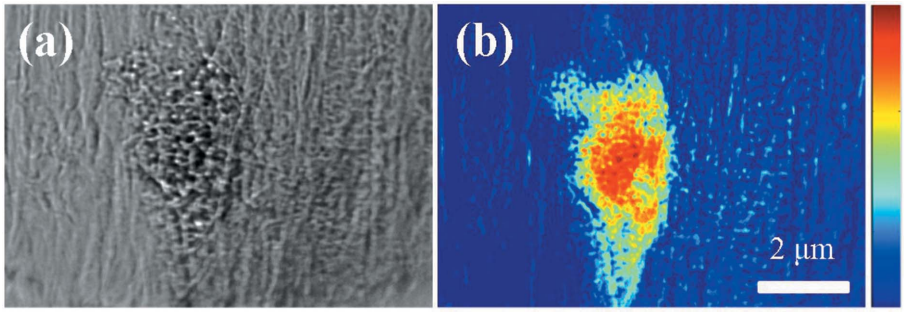

Figure 7
(*a*) Zernike phase contrast image and (*b*) pseudocolor iron-sensitive image of maize roots.

($LiCoO_2$) design found in consumer electronics, but offer longer lifetimes as well as inherently greater safety. With these advantages, LFP batteries are finding a number of roles in vehicle and backup-power applications. LFP-material imaging by XANES has been reported to be an effective method for identification of the actual status of the lithium ion with phase transformation of the iron core level (Boesenberg *et al.*, 2013; Wang *et al.*, 2014; Pongha *et al.*, 2015). Preliminarily in the present experimentation, full-field XANES imaging of LFP cathode material by scanning X-ray energy at the Fe *K*-edge from 7100 to 7160 eV in 0.5 eV steps was carried out. For each energy, a transmission image is normalized with its flat-field image in order to obtain a reliable XANES spectra. The flat field was acquired by retracting the sample in the beam path using a high-precision piezo stage. Moreover, in order to improve the signal-to-noise, an average image of ten normalized images at each energy was used. A XANES stack consisting of a series of the average image and XANES spectra can then be extracted for each pixel of the image. LFP samples had been prepared by a simple solid-state reaction process entailing mixing with carbon black in a weight ratio of 60:40. Discharged *ex situ* cathode samples had been prepared by cell-discharging over an applied voltage of 4.2 V at room temperature. Fig. 8 shows the XANES spectra (left) and pseudocolor TXM image (right) at 7140 eV of the fully discharged LFP cathode. The XANES spectra, as obtained at two representative points [*i.e.* the presumed shell (B) and core (A) positions], showed evident difference. It is well known that lithium extraction from the fully discharged state generally exhibits the structure of the $LiFePO_4$ core and the $FePO_4$ shell. According to the reference standard spectra (inset), we could estimate which part was closer to the $LiFePO_4$ or $FePO_4$ phase. Also we could determine that, compared with the shell (B), the core (A) was in the mixed phase. Certainly, as indicated here, XANES phase analysis is an attractive method for elucidation of the reaction mechanism of typical lithium-ion battery material. Future developments of the spectroscopic setup will focus on *in operando* experimentation (battery work) and automated data acquisition by combined XANES tomography.

4. Conclusions

Herein we have presented the specifications and various details on the newly upgraded 7C sXNI beamline at PLS-II. Also, we have provided the early commissioning results for spectroscopic nano-imaging. In order to obtain trustworthy XANES images at nano-resolution, we modified the DCM, installing focusing plane mirrors and a beam-position feedback system. To demonstrate chemical-sensitive imaging, we took TXM images of iron accumulation in live maize roots as well as XANES images of iron's phase distribution in the lithium–iron–phosphate cathode of a lithium-ion battery. The TXM–XANES technique has the unique capability of producing chemical composition images of micrometer-sized battery materials at different phase-transformation stages, with high spatial and chemical resolution. This paper can be utilized as an introduction to a newly available XANES imaging beamline.

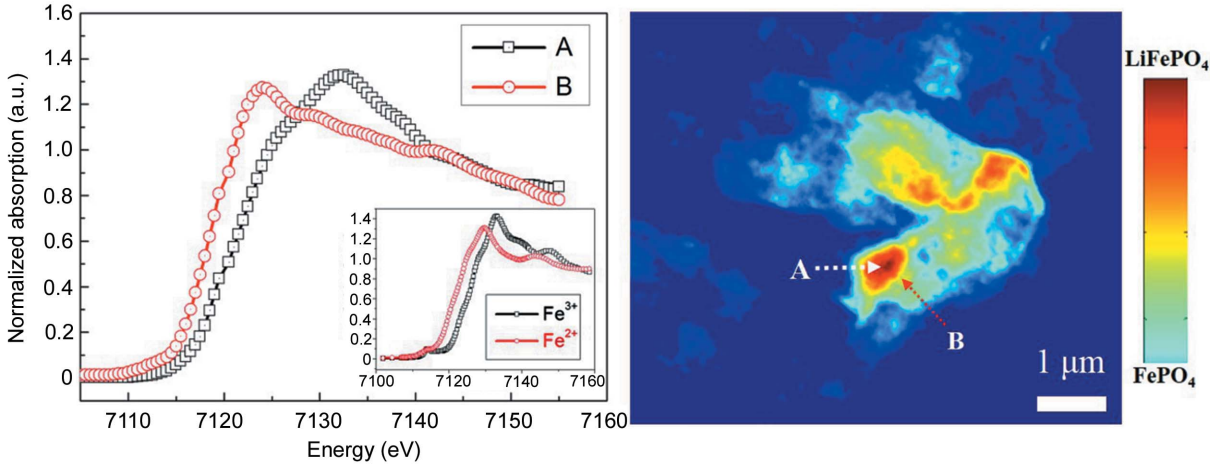

Figure 8
XANES spectra (left) and pseudocolor TXM image (right) of the LFP cathode.

Acknowledgements

This research was supported by the Basic Science Research Program through the National Research Foundation of Korea (NRF) and the Creative Economy Leading Technology Development Program. The development of the electronic instrumentation was supported by the research laboratory of Topkorea Co. Ltd.

Funding information

Funding for this research was provided by: Ministry of Science, ICT and Future Planning (2017R1A2B1002457, 2017R1C1B1011518) and the Gyeongsangbuk-Do and Gyeongbuk Science & Technology Promotion Center of Korea (SF316002A).

References

Andrade, V. D., Deriy, A., Wojcik, M. J., Gursoy, D., Shu, D., Fezzaa, K. & Carlo, F. D. (2016). *SPIE Newsroom*, doi:10.1117/2.1201604.006461.

Bauer, S., de Biasi, L., Glatthaar, S., Toukam, L., Gesswein, H. & Baumbach, T. (2015). *Phys. Chem. Chem. Phys.* **17**, 16388–16397.

Boesenberg, U., Meirer, F., Liu, Y., Shukla, A. K., Dell'Anna, R., Tyliszczak, T., Chen, G., Andrews, J. C., Richardson, T. J., Kostecki, R. & Cabana, J. (2013). *Chem. Mater.* **25**, 1664–1672.

Chen, T.-Y., Chen, Y.-T., Wang, C.-L., Kempson, I. M., Lee, W.-K., Chu, Y.-S., Hwu, Y. & Margaritondo, G. (2011). *Opt. Express*, **19**, 19919–19924.

Grew, K. N., Chu, Y. S., Yi, J., Peracchio, A. A., Izzo, J. R. Jr, Hwu, Y., De Carlo, F. & Chiu, W. K. S. (2010). *J. Electrochem. Soc.* **157**, B783–B792.

Kuppan, S., Xu, Y., Liu, Y. & Chen, G. (2017). *Nat. Commun.* **8**, 14309.

Kwon, I.-H., Lim, J. & Hong, C.-K. (2016). *J. Synchrotron Rad.* **23**, 1237–1240.

Lim, J., Kim, H. & Park, S. Y. (2014). *J. Synchrotron Rad.* **21**, 827–831.

Liu, Y., Meirer, F., Williams, P. A., Wang, J., Andrews, J. C. & Pianetta, P. (2012). *J. Synchrotron Rad.* **19**, 281–287.

Meirer, F., Cabana, J., Liu, Y., Mehta, A., Andrews, J. C. & Pianetta, P. (2011). *J. Synchrotron Rad.* **18**, 773–781.

Nazaretski, E., Lauer, K., Yan, H., Bouet, N., Zhou, J., Conley, R., Huang, X., Xu, W., Lu, M., Gofron, K., Kalbfleisch, S., Wagner, U., Rau, C. & Chu, Y. S. (2015). *J. Synchrotron Rad.* **22**, 336–341.

Pongha, S., Seekoaon, B., Limphirat, W., Kidkhunthod, P., Srilomsak, S., Chiang, Y.-M. & Meethong, N. (2015). *Adv. Energ. Mater.* **5**, 1500663.

Rau, C., Somogyi, A. & Simionovici, A. (2003). *Nucl. Instrum. Methods Phys. Res. B*, **200**, 444–450.

Shapiro, D. A., Yu, Y. S., Tyliszczak, T., Cabana, J., Celestre, R., Chao, W., Kaznatcheev, K., Kilcoyne, A. L. D., Maia, F., Marchesini, S., Meng, Y. S., Warwick, T., Yang, L. L. & Padmore, H. A. (2014). *Nat. Photon.* **8**, 765–769.

Vila-Comamala, J., Pan, Y., Lombardo, J., Harris, W. M., Chiu, W. K., David, C. & Wang, Y. (2012). *J. Synchrotron Rad.* **19**, 705–709.

Wang, J., Chen-Wiegart, Y. & Wang, J. (2014). *Nat. Commun.* **5**, 4570.